

Assessing form-dependent optical scattering at vacuum- and extreme-ultraviolet wavelengths off nanostructures with two-dimensional periodicity

Bryan M. Barnes,* Mark-Alexander Henn, Martin Y. Sohn, Hui Zhou, and Richard M. Silver

Nanoscale Device Characterization Division, Physical Measurement Laboratory,

National Institute of Standards and Technology,

100 Bureau Dr MS 8212, Gaithersburg, MD 20878-8212, USA[†]

(Dated: July 1, 2019)

Abstract

Form birefringence, where the orientation of periodic structures yields effective refractive index differences between orthogonal polarizations, is integral to multidimensional optical data storage, is apparent for certain metamaterials, yet is also critical to the inspection of periodic devices in nanoelectronics. A traditional assumption behind form birefringence - that the wavelength is larger than the periodicity - challenges several applications at shorter wavelengths. In this paper, the form dependence of high spatial-frequency scattering off structures with two-dimensional periodicity is numerically assessed among deep-, vacuum-, and extreme-ultraviolet illumination wavelengths (DUV, VUV, EUV). At each wavelength, the available optical hardware is incorporated as a constraint and the impact of known laboratory source intensities is addressed. Evaluations are presented for both ideal periodic arrays and arrays with an added bridging defect that breaks the local periodic symmetry. Form-dependent scattering (FDS) intensity ratios in the ideal case decrease with wavelength in the DUV and VUV, but dramatically increase for the 47 nm EUV wavelength, due to the wavelength-dependent optical properties of the conformal layers modeled. This increase at 47 nm wavelength shifts the ideal polarization for FDS off the bridging defect and enhances sensitivity to these patterning faults. The results of these realistic simulations in this challenging wavelength range should be extensible, not only to structures in nanoelectronics, but also to emerging engineered optical materials for DUV and shorter wavelengths.

PACS numbers: 42.25.Fx, 78.20.Fm, 42.30.Va, 02.70.Bf

* bryan.barnes@nist.gov

I. INTRODUCTION

Form birefringence is the induced difference, due to geometrical factors, in refractive index between different polarizations of light traveling through or reflecting off a structured material. It is found in nature [1, 2], observed in anisotropically nanostructured silicon [3, 4], and also created using microscale patterning [5–8] (for micrometer and infrared wavelengths) and nanoscale fabrication [9, 10] (for visible and ultraviolet wavelengths). Non-resonant metamaterials with a effective negative index of refraction have been realized utilizing form birefringence [6]. It has also been integral to characterizing periodic nanoelectronic devices [11]. These examples follow a traditional understanding of form birefringence, that it arises from “an ordered arrangement of similar particles of optically isotropic material whose size is large compared with the dimensions of molecules, but small compared with the wavelength of light [12].” Among metamaterials that inherently exhibit artificial optical properties due to individual resonant scatterers, some additionally exhibit form birefringence [13] while others utilize nominally form-birefringent elements augmented to resonant [14, 15].

Form birefringence is accounted for through effective medium approximations (EMA), and Fig. 1(a,b) illustrates schematically the treatment of a form-birefringent material using an EMA. For typical periodic structures, if the periodic spacing, p , is much less than the wavelength of the incident light, λ , no higher-order scattering is produced and the birefringence can be expressed as

$$\epsilon_{\perp} - \epsilon_{\parallel} \geq 0, \quad (1)$$

where ϵ_{\perp} and ϵ_{\parallel} are the effective dielectric functions for two orthogonal linear polarizations.

While the form birefringence of structures with a periodicity p is well-described when $p \ll \lambda$, the polarization-dependent optical response is more ambiguous if $\lambda \leq p$. A notable exception, however, are metagratings, which are comprised of periodic sets of dissimilar elements designed to engineer the local phase [16]. The periodicity of these sets may exceed λ , yet enable perfect engineered reflection [17]. Popov *et al.* controlled surface impedances on each of N elements in their set to selectively control which of the potential N plane waves

[†] Certain commercial materials are identified in this paper in order to specify the experimental procedure adequately. Such identification is not intended to imply recommendation or endorsement by the National Institute of Standards and Technology, nor is it intended to imply that the materials are necessarily the best available for the purpose.

would be scattered off that set [18]. Liu *et al.* further proposed tuning both reactive and absorptive properties at different frequencies and incident angles for both linear orthogonal polarizations of incident wave [19]. Wavelengths for these exceptional structures range, thus far, from the infrared to longer wavelengths.

Currently, periodic systems illuminated using visible and shorter wavelengths for which $p \approx \lambda$ will exhibit higher-order diffraction. Many modern fabricated optical materials feature structured periodicities p that begin to approach λ . Smith *et al.* [20] noted that an initial demonstration of a metamaterial with a negative refractive index [21] had a periodicity $p \approx \lambda/6$, and proposed approaches for maintaining an EMA for such materials. Likewise, recent activity using ultrafast laser nanostructuring in glasses [22, 23] has renewed interest in form birefringence for multidimensional optical data storage [24] with $p \approx \lambda/9$ using visible wavelengths. Another application is concentric surface-relief gratings, which create helical wavefronts upon reflection at $\lambda = 405$ nm with $p = 322$ nm [25]. As the period p continues to decrease with improved fabrication technology, λ will be reduced further to deeper ultraviolet wavelengths. With $p \approx \lambda$, both experimental measurements and electromagnetic modeling of such structures become increasingly critical.

This paper investigates numerically the scattering off arrays of nanoscale structures with two-dimensional (2-D) periodicity at even shorter wavelengths, spanning the DUV, the vacuum-ultraviolet (VUV), and the extreme-ultraviolet (EUV). While the spacing p is less than the wavelength in one direction, as illustrated in Fig. 1(c) these structures

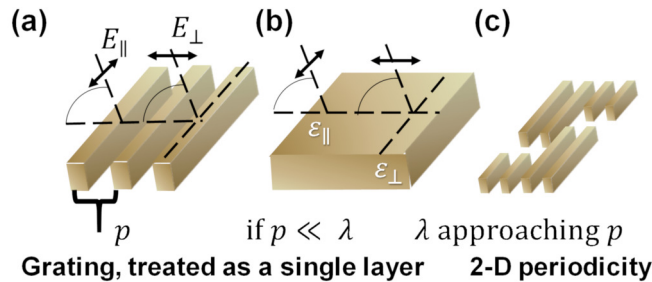


FIG. 1. Schematic representations of reflecting and scattering structures. (a) Periodic structure that due to form birefringence reflects transverse-electric (i.e., \parallel to grating as shown) polarized light differently than transverse-magnetic (i.e., \perp) polarized light (as $p \ll \lambda$). (b) Effective medium approximation. (c) Structure types considered in this present work, with λ approaching or shorter than p .

have lengths and spacings, specified in the next Section, in the orthogonal direction that yield higher-order scattering at DUV, VUV, and EUV wavelengths. In this wavelength regime, the simpler treatment of form-birefringent reflectivity using an EMA must be replaced by an assessment of form-dependent scattering (FDS) with high-frequency spatial content from an inhomogeneous layer. In experiments at visible and DUV wavelengths, our group has successfully measured deep-subwavelength structures that scatter such high-frequency spatial content on a high-magnification platform in the laboratory [26–34]; others notably have measured structure-based birefringence using linearly-polarized x-rays in synchrotron-based experiments, imaging the local orientational properties of brominated organic molecules [35]. For these simulations throughout the ultraviolet, wavelength-appropriate optical configurations are presented and non-synchrotron light sources are presumed due to their potential technological impact. Image intensities from these arrays are compared as functions of wavelength and polarization. Methods for and challenges to imaging at 13 nm, 47 nm, 122 nm, 157 nm, and 193 nm wavelengths are incorporated into this analysis.

These arrays, defined in Section II, are technologically relevant in nanoelectronics, and simulations include scattering both with and without the presence of an undesired non-periodic bridging defect. Scattering intensities with respect to linear polarization are presented for the two-dimensional periodic array in Section III. The effects of FDS upon the scattered intensity are studied as the wavelength decreases into the VUV and EUV, including strong FDS intensity at $\lambda = 47$ nm for the periodic array. Section IV presents the FDS after the addition of the bridging defect. This allows examination of the wavelength extensibility of the challenging problem of identifying sub-10 nm wide imperfections with optics, as is currently employed in nanoelectronics fabrication (i.e., defect inspection) using $\lambda > 190$ nm [36, 37]. At all wavelengths, FDS can be observed from the bridge if enough photons are hitting the sample, but $\lambda = 47$ nm is notable for the low number of photons required to attain the signal and is unique among these five wavelengths as its optimal polarization axis for FDS is defined by the array and not by the bridge direction as has been calculated for DUV and longer wavelengths [30–32, 38, 39]. Note also, several other defect types have been recently explored at ultraviolet and longer wavelengths elsewhere for their effects upon form birefringence and polarized optical scattering [40, 41]. While the geometries and materials for the patterned devices presented in this paper are optimized

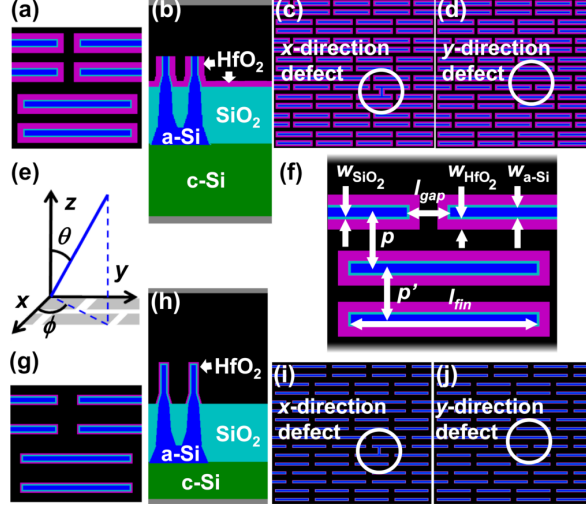


FIG. 2. Cross-sections of the two geometries of periodic nanostructures used in these simulations (a) x - y cross-section of a unit cell (UC) for Geometry 1 (b) y - z cross-section of Geometry 1, (c, d) x - y cross-sections of a $4 \text{ UC} \times 4 \text{ UC}$ array containing an isolated bridging defect. (e) Definition of axes with respect to line directions. (f) Key lengths that define the structure and its periodicity, with values in Table I. Panels (g-j) represent Geometry 2, mirroring the cross-sections shown in panels (a-d) for Geometry 1.

for a specific technological application, the simulation methodologies presented should be applicable not only for nanoelectronics-derived structures but also to other optical materials in the DUV, VUV, and EUV.

II. SIMULATIONS AND IMAGE FORMATION

To quantitatively assess form-dependent optical scattering, electromagnetic scattering calculations have been performed using two similar geometrical layouts of technologically relevant features with 2-D periodicity. As shown in Fig. 2, both layouts are comprised of conformally coated amorphous Si (a-Si) structures on a crystalline Si (c-Si) substrate with a SiO_2 layer. These geometries are based on designs of fin field-effect transistors [42] to represent key trends in nanoelectronics. The widths of the a-Si features are on average 7 nm and 6 nm for the two geometries, respectively, with a-Si heights 42 nm and 52 nm above a 78 nm thick SiO_2 layer coating the c-Si substrate. Also shown in Fig. 2 are two isolated, sub-wavelength bridging defects that will alter the scattering off the nominal structure.

TABLE I. Key dimensions for the two geometries shown in Fig. 2 using variables defined in Fig. 2(f), where $\Delta(x_{\text{fin}})$ (not shown) is the offset between the centers of lines spaced by p . Unit cell dimensions are $\{l_{\text{fin}} + l_{\text{gap}}, 2p + 2p'\}$. Fin widths are averaged. All dimensions are in nm.

Geometry	p	p'	l_{fin}	l_{gap}	$\Delta(x_{\text{fin}})$	$w_{\text{a-Si}}$	w_{SiO_2}	w_{HfO_2}
1	44	40	146	34	102	7	2	8
2	42	42	146	34	102	6	2	2

Information on the two-dimensional periodicity and linewidth for each geometry appear in Table I, and the complete simulation geometries with and without these defects are provided for download as Supplemental Information [43]. The complex index of refraction, ($\tilde{n} = n + ik$) for each material is wavelength-dependent and their respective values are provided in Table II. To determine how the properties of these materials impact the scattered intensities, additional simulations have been performed using line-space arrays with and without the layers above the SiO_2 that are conformal to the a-Si structures.

An in-house implementation in three-dimensional (3-D) space of the finite-difference time domain (FDTD) method has been utilized for each of the five wavelengths. Our 3-D FDTD implementation, is well-validated against experiments, [30, 32], against analytical solutions [44], and uses a cubic Yee cell grid upon which the electric field and magnetic field are propagated with respect to time [45]. Once a steady-state solution is achieved, the scattering approximates that from a single plane wave (SPW) of illumination at one linear polarization. Each FDTD simulation yields the electric field after diffraction, refraction, and scattering for each incident SPW. The present study has required the identification of wavelength-dependent FDTD parameters such as the simulation domain size and cell grid size; a brief description of necessary considerations for FDTD at multiple UV wavelengths is provided as Appendix A. This 3-D FDTD code accomodates calculations in 2-D space, e.g., the line-space arrays.

An assessment of the optical instrumentation available at each wavelength is also provided as Appendix B. Key findings include the maximum numerical aperture (NA) for $\lambda \geq 157$ nm that are considered here, $\text{NA} = 0.95$ with brightfield illumination (BF). For $\lambda \leq 122$ nm there is often an obscuration on-axis as only reflective optics are practical, limiting the NA range to $\text{NA} = 0.2$ to 0.5 but but allowing for either darkfield (DF) or brightfield illumination.

TABLE II. Optical constants for key materials used in nanoelectronics manufacturing, including amorphous and crystalline Si.

λ (nm)	a-Si ^a		c-Si ^b		SiO ₂ ^c		HfO ₂ ^d	
	n	k	n	k	n	k	n	k
13	1	0.02	1.03	0.00113	0.98	0.01	0.97	0.0157
47	0.88	6.58	0.803	1.78	0.62	0.30	0.58	0.06
122	0.44	1.10	0.295	1.32	2.62	0.93	1.59	1.69
157	0.67	1.63	0.49	2.04	1.80	0	2.36	1.22
193	1.16	1.29	0.88	2.80	1.66	0	2.98	0.43

^a based on Ref. 46.

^b based on Ref. 47.

^c based on Ref. 48.

^d based on Refs. 49–51.

These ranges are illustrated as Fig. 3, including the positions in the back focal plane of the objective lens at which multiple SPW computations are performed to simulate these finite apertures.

Each FDTD simulation yields the Fourier scattering components for each SPW. These

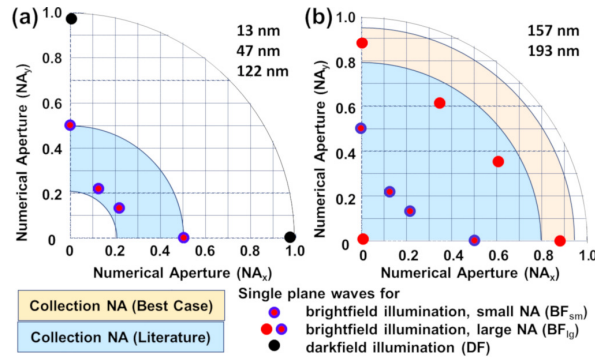


FIG. 3. Realistic illumination and collection numerical apertures (INA, CNA) (a) CNA range from $NA = 0.2 - 0.5$ for 13 nm, 47 nm, and 122 nm wavelengths with both small NA-range bright-field (BF_{sm}), grazing-angle dark-field (DF), and normal-incidence dark-field (BF_{lg}) illumination. (b) CNA ranges from $NA = 0 - 0.95$ as a best-case for long VUV and DUV wavelengths for BF_{lg} illumination. Note, BF_{sm} is a subset of BF_{lg} in (b) and is used in Section III at all λ for uniformity.

are combined using an inverse Fourier transform, before fields are summed over multiple SPWs following Fig. 3 for DF and BF_{sm} (for $\lambda = 13 \text{ nm}$ to 122 nm), BF_{sm} and BF_{lg} for $\lambda \geq 157 \text{ nm}$. Representative images appear in Fig. 4 for each of the five wavelengths, with and without the bridging defect embedded in the periodic set of features. Structures containing the isolated bridging defect are termed "perturbed" while the nominal structure deemed "ideal". As shown in Fig. 4(c), the imaged intensity contrast due to this bridging defect can be enhanced by subtracting the image of the ideal structure from the image of the perturbed structure, yielding a differential image. Often this image is processed using its absolute value and referred to as the absolute value differential image (AVDI). The ideal images are analysed for FDS and potential similarities to form-birefringent materials in Section III. AVDIs are processed in Section IV to assess the FDS from a bridging defect, yielding an analysis of the potential applications for these results.

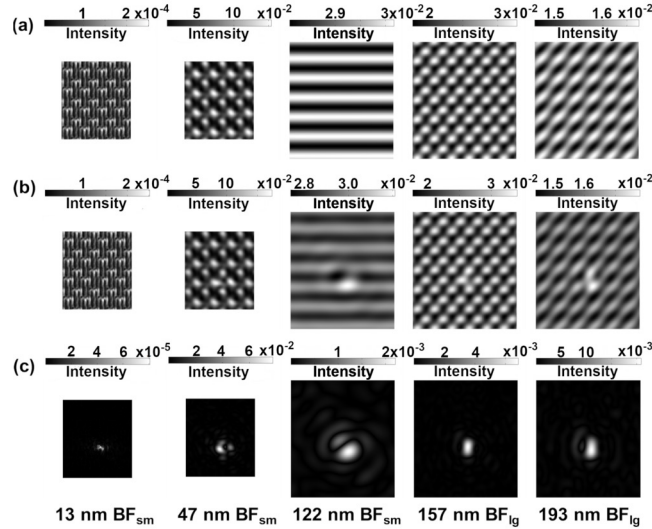


FIG. 4. Illustrations of imaging and differential imaging. Incident intensity in the simulations is normalized to be unitless with $I_0 \equiv 1$. (a) Simulated image of the 2-D periodic features, identified in the text as "ideal". (b) Simulated images of the ideal structure with an embedded bridging defect, identified as "perturbed". (c) Absolute-value differential images (AVDIs) using the ideal and perturbed images. The incident light for these figures is polarized parallel to the long axis of the ideal structure (the Y axis as defined in Fig. 2).

III. OPTICAL RESPONSE FROM PERIODIC STRUCTURES IN THE VUV AND EUV

Two dominant factors influence the optical scattering off these ideal periodic structures in the DUV, VUV, and EUV: the intrinsic optical constants of the materials and the extrinsic scattering effects due to form, which includes the structures' periodic spacing(s). To assess the roles of both factors upon the FDS among wavelengths, the illumination and collection configurations are limited in this section to the BF_{sm} condition as defined in Fig. 3, the shared illumination scheme common to all five wavelengths.

Data analysis of the resultant images is challenging due to the higher-frequency spatial content in the images. Note that if our simulated high-magnification optical platform

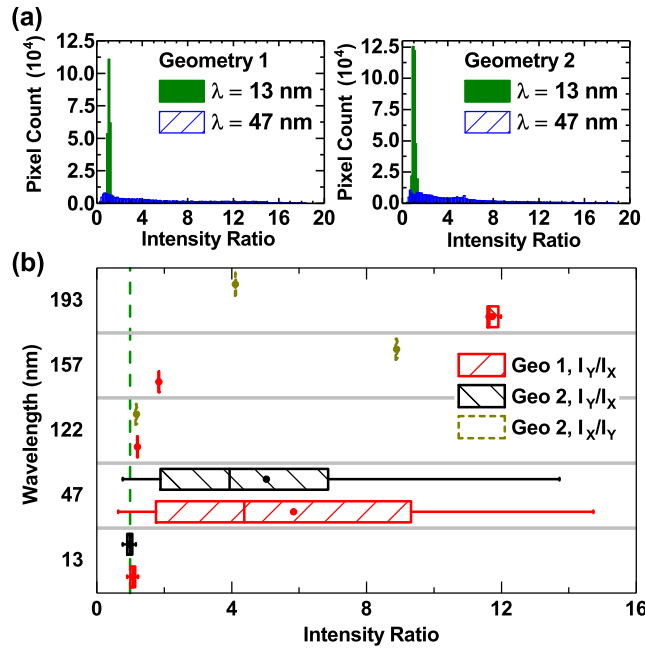


FIG. 5. Distributions on the intensity ratio between image pairs simulated using orthogonal, linearly polarized illumination calculated on a pixel-by-pixel basis. (a) Intensity ratio distributions at $\lambda = 13$ nm and $\lambda = 47$ nm (b) Box and whisker plots of the intensity ratio distributions at each wavelength and geometry. Whisker bars denote the range between the 5th and 95th percentiles of the distributions while the box plot covers the 25th to 75th percentiles. Mean intensity ratios are denoted with a circle. A ratio of 1 (green dotted vertical line) indicates no detectable FDS. All distributions computed are relatively narrow except at $\lambda = 47$ nm.

collected images of a truly form-birefringent material, the images would have no high-frequency content but the image's flat intensity would still vary with incident polarization. Such an image could be reduced in practice to a single pixel and using normalization techniques [26, 29] could be converted to a reflectivity. The analysis may be further simplified using a *reflectivity ratio*, dividing the separate reflectivities from orthogonal linear polarizations. Note, alternatives metrics such as determination of phase differences [52] may also be utilized for $p \ll \lambda$.

However with 2-D periodicity and $p \lesssim \lambda$, FDTD simulations yield evidence in each incident SPW of both higher-order diffracted and scattered Fourier components of the electric field, which are combined using an inverse Fourier transform before the resulting simulated image is constructed using multiple plane waves. These images cannot be reduced to a single pixel and the differences in scattered intensity with incident polarization are to be assessed as *pixel-by-pixel intensity ratios*. Using an image from both incident orthogonal polarizations, one obtains *pixel-by-pixel distributions*; the distributions for $\lambda = 13$ nm and $\lambda = 47$ nm are shown as Fig. 5(a). The key result for $\lambda = 13$ nm from Fig. 5(a) is that the intensity ratio, $R_{signal} = I_{signal_{Y_{pol.}}} / I_{signal_{X_{pol.}}} = I_Y / I_X$ calculated pixel-by-pixel, yields a narrow distribution centered close to unity for both geometries, indicating that although R_{signal} can vary within the image, there is little meaningful FDS. Contrast this result with those for $\lambda = 47$ nm in Fig. 5(a). The distributions are wide, indicating a large variance in the ratio across the set of pixels forming each image, with $\overline{R_{signal}} \approx 4$. From this distribution of intensity ratios, the FDS appears relatively strong.

To assess these distributions across all five wavelengths, a box-and-whisker plot is provided as Fig. 5(b). A dashed vertical line denotes the absence of form-dependent scattered intensity where $I_X = I_Y$. As the wavelength decreases into the VUV and approaches the periodic spacing length, FDS is greatly reduced irrespective of optical constants. The distributions at $\lambda > 122$ nm are relatively narrow, similar to that at $\lambda = 13$ nm, qualitatively emulating the scalar ratio between reflectances expected for true form birefringence. Especially for Geometry 1, the mean intensity ratio appears to converge to unity as λ approaches 122 nm. Note, however, that in Fig. 5(b), the pixel-by-pixel intensity ratio is inverted ($I_X / I_Y > 1$) for Geometry 2 and $\lambda \geq 122$ nm.

As the periodic silicon features vary minimally between the two geometries, it is a reasonable assumption that the optical properties in Table II drive the magnitude of the

TABLE III. Ratio of $\bar{I}(I_Y)/\bar{I}(I_X)$ for line/space arrays as simulated at the five simulation wavelengths using Table II. Coatings “as shown” corresponds to all materials in Figs. 2(b,h) while “none” represents the removal of the SiO₂ and HfO₂ conformal to the a-Si structure.

Geometry	Coatings	λ				
		13 nm	47 nm	122 nm	157 nm	193 nm
1	as shown	1.1	9.6	1.2	1.9	5.7
	none	1.0	3.4	2.6	1.7	1.0
1 ^a	as shown	1.1	11.1	1.2	1.7	5.0
	none	1.0	2.6	2.8	1.8	1.0
2	as shown	1.1	41.6	0.4	0.4	0.7
	none	1.1	6.1	0.8	1.2	2.0

^a Pitch altered from Table I to $p = p' = 42$ nm.

intensity ratio and the relative weights between I_X and I_Y , as Geometry 1 has the thicker HfO₂ conformal film on the fins and SiO₂ surface as compared to the mostly SiO₂ surface for Geometry 2. These similarities reduce the likelihood that the differences in form-dependent scattering reported here is due to localized phase control, the basis of a metagrating reported by Khorasaninejad and Capasso [16]. They tailored the individual widths of periodic sets of subwavelength-spaced fins to passively alter the phase, as such fins can function as dielectric ridge waveguides. To validate the importance of wavelength-dependent materials properties, 2-D FDTD has been performed for similar structures with and without these conformal layers at the fins, with intensity ratios provided as Table III. Comparing the 2-D FDTD FDS of the structures with conformal layers against the results in Fig. 5(b), many trends persist between the 2-D and 3-D FDTD. For $\lambda \geq 122$ nm the ratio of mean intensities appears to converge towards $\bar{I}_Y/\bar{I}_X = 1$, and again the preferred linear polarization differs between Geometry 1 (Y-polarized light) and Geometry 2 (X-polarized) in this wavelength range.

Note however that as the conformal layers are removed from the fins of the line-space array, the ratio $\bar{I}(I_Y)/\bar{I}(I_X)$ varies. Without either the SiO₂ or HfO₂ conformal fin coatings, most ratios converge toward $\bar{I}(I_Y)/\bar{I}(I_X) = 1$. Notable exceptions include the increase in this ratio for Geometry 1 and 122 nm wavelength, and the increase for Geometry 2 at 193

nm wavelength. The optimal linear polarization direction changes also for Geometry 1, 193 nm wavelength and Geometry 2, 157 nm wavelength. Setting $p = p' = 42$ nm for Geometry 1 has only slight effects on these ratios relative to $p = 44$ nm, $p' = 40$ nm. Therefore, materials properties dominate the magnitude and affect the preferred polarization direction for FDS in the VUV and EUV. Proper choices of λ with respect to p as well as $\tilde{n}(\lambda)$ are critical to optimizing FDS at these wavelengths.

IV. FORM-DEPENDENT SCATTERING OFF A BRIDGING DEFECT

A. Imaging and Analysis

The methods presented above for comparing the FDS off periodic arrays utilize the entirety of the image, pixel-by-pixel. More sophisticated steps are required to analyse the measurable scattered intensity from periodic features that include a defect. In this work, an aperiodic defect that bridges adjacent nominal features has been added. Realistic illumination conditions, collection conditions, and image noise must be incorporated in the study and a metric developed to assess the potential FDS.

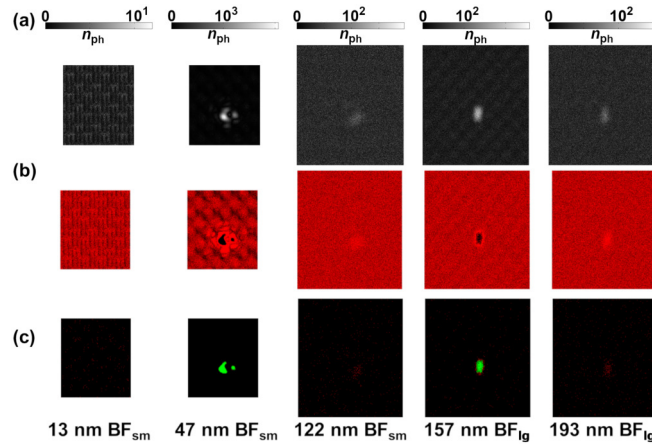


FIG. 6. Illustration of signal identification using example data from Fig. 4 (a) AVDI after shot noise applied to ideal and perturbed images. Intensity is here represented in the number of photon counts, n_{ph} . (b) Initial binary mask from watershed intensity thresholding. Red pixels are below the threshold, black pixels above. (c) Mask with an additional area threshold applied; green pixels have sufficient area. Images are to scale.

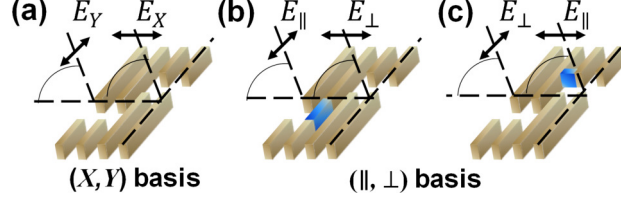


FIG. 7. Schematic representations of ideal and perturbed scattering structures. (a) Ideal structure analysed in Sec. III with polarization basis (X, Y) with respect to sample (b,c) Perturbed structures analysed in this section, with polarization basis set $(||, \perp)$ relative to the bridging defect.

The image noise applied in this study is shot noise, a persistent problem in low-light applications as is expected in the VUV and EUV. Shot noise is intensity-dependent, and to apply shot noise the photon count at the sample n_{ph} must be provided. Using $n_{\text{ph}} = 6.4 \times 10^3$, shot noise is applied to the images in Fig. 4(a,b) to yield the AVDI in Fig. 6(a). Currently available magnitudes for $n_{\text{ph}}(\lambda)$ are estimated in Appendix C and their implications will be discussed later.

The signal due to the scattering from an added bridging defect is readily observable in Fig. 6(a) at 47 nm and 157 nm wavelengths. Figure 6(b,c) illustrates how computationally a signal can be extracted from the AVDI with all remaining pixels characterized as noise. The criteria for separating “signal” from “noise” require definition, and experimental experience [30–32] in imaging such imperfections for the nanoelectronics industry leads us to propose two thresholds. First, a binary mask is constructed of those pixels with intensities $I > 5 \sigma_{\text{AVDI}}$, the standard deviation across the whole AVDI, as shown in Fig. 6. Second, the contiguous regions of the mask are analyzed and areas where $A \geq (3 \text{ nm})\lambda$ are deemed as signal with smaller areas also defined as noise. These area and intensity thresholds utilize the information content in the AVDIs by incorporating our prior information about the scattering volume. The wavelength is included in the area threshold to unbiased the signal-to-noise ratio (SNR) against the smaller scattering volumes that arise at shorter wavelengths from such added features. Once the pixels deemed to be signal have been identified, the intensities of these pixels may be averaged and utilized as a signal-based metric $\overline{I_{\text{signal}}}$. This single-valued metric allows comparisons between the differential images from two orthogonal linear polarizations.

The optimal illumination scheme among DF, BF_{sm} , or BF_{lg} from Fig. 3 is determined

from maximizing $\overline{I_{\text{signal}}}$ over a wide range of possible photon counts, n_{ph} . For $\lambda = 13$ nm, DF illumination yields the strongest differential signal, while BF_{sm} proves the better illumination scheme for the 47 nm and 122 nm wavelengths. With larger NA available for $\lambda \geq 157$ nm, BF_{lg} yields a greater $\overline{I_{\text{signal}}}$ for that wavelength range. This optimization requires a re-evaluation of the polarization basis used thus far, the (X,Y) basis as shown in Fig. 7(a). Once a bridging defect is introduced as in Fig. 7(b,c), another polarization basis may be defined by the long axis of the *bridging* feature. The optimal polarization at each value of n_{ph} is determined over several orders-of-magnitude as required to cover the range of available and potential source intensities.

As in Section III, the ratio between two signals collected at different orthogonal polarizations is used to identify and characterize FDS. Here the ratio is defined as

$$R_{\text{signal}} = \frac{\overline{I_{\text{signal}_{\parallel}}}}{\overline{I_{\text{signal}_{\perp}}}}, \quad (2)$$

where the (\parallel, \perp) basis is defined as in Fig. 7. Figure 8 yields R_{signal} as functions of geometry, bridging defect direction, wavelength, and photon count. There are stark differences between the 47 nm wavelength and the other simulation wavelengths. The minimum photon count required to have a measurable R_{signal} value is similar across the wavelengths except for $\lambda = 47$ nm. For most wavelengths, the majority of data points in Fig. 8 are well-optimized by defining the linear polarization in the (\parallel, \perp) basis with most values $R_{\text{signal}} > 1$. The few values where $R_{\text{signal}} \approx 1$ are found for Geometry 1 with the bridging defect in the X-direction, suggesting the influence of the conformal HfO₂ film's optical properties upon Geometry 1 in the $\lambda \geq 122$ nm range.

At 47 nm wavelength, the materials effects observed in Sec. III impact the optimal polarization axis for the bridging defect. Specifically, as $R_{\text{signal}} < 1$ in Fig. 8(a) while $R_{\text{signal}} > 1$ for Fig. 8(b), the polarization basis is not relative to the bridging defect for $\lambda = 47$ nm. The FDS of the defect is optimized along the axis of the set of 3-D periodic features, which follows from the large intensity ratios for both geometries of the set of ideal features as shown in Fig. 5 if the illumination is aligned along the Y-direction. Determining ideal combinations of λ and its $\tilde{n}(\lambda)$ to optimize FDS from an ideal array may similarly impact the signal strength and preferred linear polarization for measuring oriented imperfections in such arrays.

B. Applications of Form-Dependent Scattering

For these selected geometries, FDS was observed for the ideal periodic array using 47 nm, 157 nm, and 193 nm wavelengths, but all wavelengths show some degree of FDS for the bridging defect with sufficient photon count, even in the presence of shot noise. The general applicability of DUV, VUV, and EUV wavelengths to periodic nanoscale arrays lies beyond the scope of this paper. Likewise, the optical response across all wavelengths to an

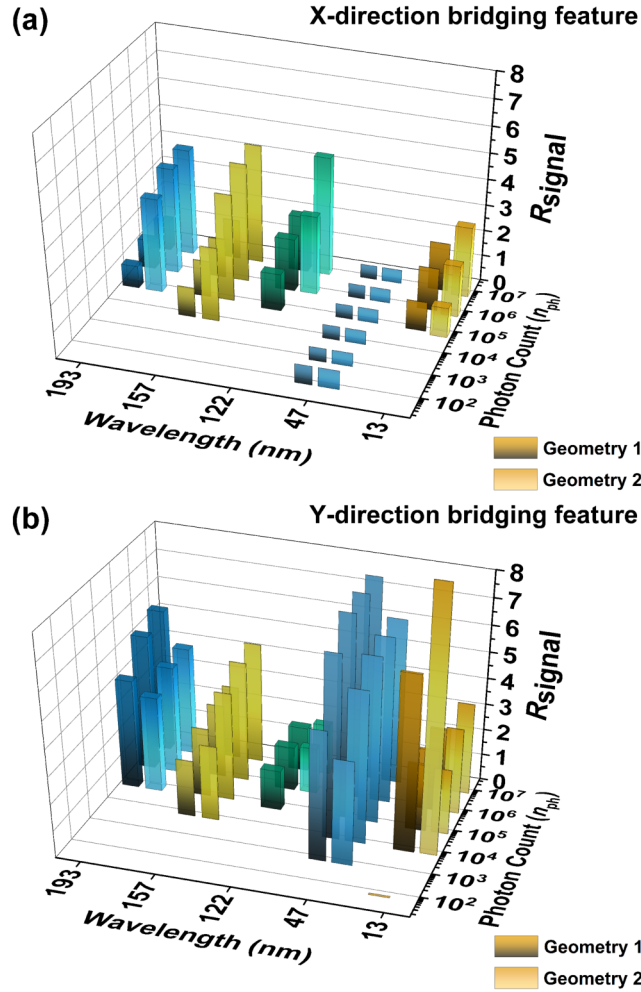


FIG. 8. Signal intensity ratios from differential image pairs simulated using orthogonal, linearly polarized illumination. These plots illustrate the ratios as functions of geometry, linear polarization, and photon count. A ratio of 1 indicates no detectable FDS. Bridging feature is aligned along the (a) X-direction and (b) Y-direction. For each wavelength, the pairs of bars represent values for Geometry 1 on the left, Geometry 2 on the right.

aperiodic structure suggests that further simulation study is required to assess the resonant response for properly scaled-down, aperiodic form-birefringent structures such as the “V” or “wedge” shaped nanoantennas used in some metasurfaces [13]. Thus while many potential applications exist for FDS or form birefringence in this wavelength range, this section briefly presents one of the many grand challenges in nanoelectronics measurement [53] and places this study’s results into context.

While it has been established that all wavelengths yield FDS from the bridging defect, the number of photons available for the task varies by wavelength. Estimates of the photon count available at each wavelength using contemporary, non-synchrotron sources are shown as Fig. 9(a). Values are derived in Appendix C. To present these simulation results while also scaling photon counts using the existing literature, another metric is introduced; a signal to noise ratio defined here as

$$\text{SNR} = \frac{\overline{I_{\text{signal}}}}{\sigma_{\text{noise}}}, \quad (3)$$

where $\overline{I_{\text{signal}}}$ is defined in Section IV and σ_{noise} is the standard deviation of the intensities at all pixels falling below the thresholds defined in Section IV. Note, by definition σ_{AVDI} differs from σ_{noise} .

Figure 9(b,c) presents the SNR as a function of wavelength and of photon count. Comparing Fig. 9(a) to Fig. 9(b,c), $\lambda = 122$ nm is unsuited to this application, returning a null value for the SNR across its available photon count range, thus not detecting the presence of the bridge. The 13 nm wavelength may yield non-zero SNR for Geometry 1 but misses the presence of the bridge (i.e., returns a null-valued SNR) in Geometry 2. Alternatively, comparing Fig. 9(a) to Fig. 9(b,c) for the 47 nm, 157 nm and 193 nm wavelengths, the bridging defect should be observed. Presently, the SNR for 193 nm is approximately equal to or surpasses the SNR at 47 nm and 157 nm wavelengths, without requiring a vacuum to propagate the light. Although the SNR difference is not dramatic between $\lambda = 157$ nm and $\lambda = 193$ nm, a slight improvement in the photon count at 157 nm wavelength may extend optics-based nanoelectronics inspection as feature dimensions continue to decrease in the near term.

The impact of the photon count may be significant if increased by one order-of-magnitude or more. The SNR value at 193 nm wavelength using current estimates of photon count are near their maximums in this analysis. However, increasing the photon count for 157 nm by one order of magnitude could increase the SNR by as much as a factor of two for these

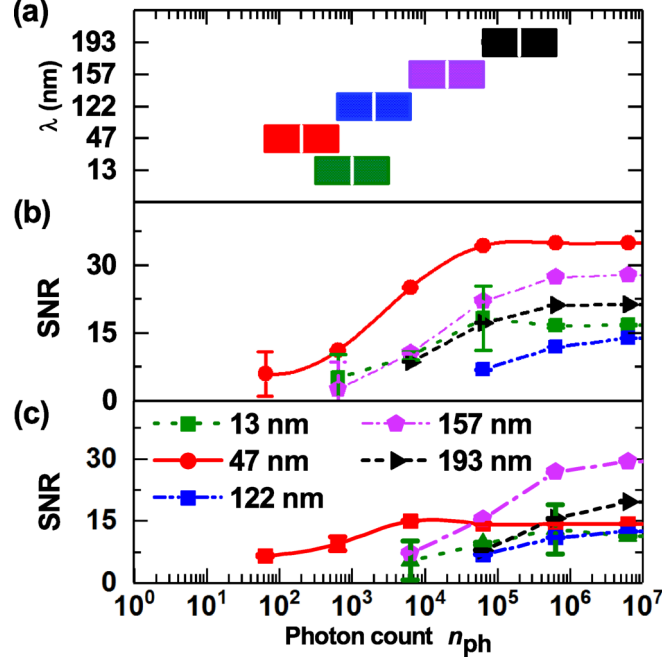


FIG. 9. Comparison of the estimated available photon counts with respect to wavelength and simulated SNR metrics. (a) Estimated available photon count from non-synchrotron sources as a function of wavelength as established in Appendix C. SNR ratios for Geometry 2 bridging defect along the (b) X-direction and (c) Y-directions. Error bars for the SNR are based off 50 realizations of the shot noise.

geometries. Notably, industrial prototyping is underway to reduce λ into the VUV [54] for this application. The most sensitive wavelength, 47 nm, also features the weakest source strength according to our analysis; a two order-of-magnitude increase in photon count would increase the SNR for $\lambda = 47$ nm by as much as a factor of 5 or more. A concerted effort to improve VUV and EUV sources could address ongoing challenges from defects sized much less than 10 nm in width.

V. CONCLUSION

The optical scattering off sets of patterned arrays with 2-D periodicity has been quantitatively calculated and compared for two geometries and five wavelengths to assess the several ways FDS is manifest in linearly polarized light at five ultraviolet wavelengths, from $\lambda = 193$ nm down to $\lambda = 13$ nm. Using DUV, VUV, and EUV wavelengths, these simulations incorporate

known limitations in source strength, optical design, and materials properties which differ greatly from what is available using visible light. FDS containing high spatial frequency content has been observed at each wavelength, in contrast to the typical form birefringence which yields only reflectance.

For periodic arrays, $\lambda = 47$ nm shows the strongest FDS due to the optical constants of the materials chosen in the simulations. For most wavelengths, if an otherwise isolated bridging defect is incorporated into this array, there is an increase in the observable scattering if the linear polarization is aligned along the direction of the bridging defect. However at 47 nm wavelength, the strong FDS of the periodic structure dominates the interplay between the scattered fields from the bridge and those from the periodic array. From the available source information and these simulations, about two orders-of-magnitude more photons are required from sources to access the full potential of this wavelength for these materials.

These results from FDS not only illustrate challenges in the use of VUV and EUV wavelengths for a specific application, but illustrate well certain difficulties as more form-birefringent materials are developed for the ultraviolet and smaller wavelengths as periodicities p continue to decrease. Although operating at times with $p > \lambda$, this study provides a key illustration of the inherent challenges and a possible solution in the simulation and numerical analysis of electromagnetic properties in the VUV and EUV. In addition, known (but not necessarily intrinsic) source intensity limitations in this critical wavelength regime have been presented. With increased source intensity, greater progress is to be expected towards overcoming these challenges to extend form-dependent applications into the VUV and EUV.

Appendix A: DUV, VUV, and EUV considerations for configuring FDTD modeling

Modeling the fields scattered by sets of features using FDTD is straightforward, but if an isolated bridging defect is embedded with such a set, that feature's unique contributions to the scattering may be lost unless the domain size is configured correctly. As our FDTD implementation is periodic in the x - y plane, the domain size must be large enough to minimize the interactions among these otherwise isolated scatterers and their periodic copies. We have previously suggested [44, 55] that the total domain x - y area should be at least $10 \lambda \times 10 \lambda$ with a cubic cell volume of at least $(\lambda/10)^3$. However, with simulation wavelengths ranging from 13 nm to 193 nm, x - y domain sizes and Δs have been varied notably as shown

in Table IV. For Geometry 1, the domain size has expanded with increasing wavelength at the cost of reduced resolution ($\Delta s \leq 2$ nm). Geometry 2 features a much thinner conformal layer, $3\Delta s = 2$ nm. Reducing Δs here is a tradeoff among resolution, domain size, execution time, and available memory (here, 64 GB). The total x - y area has been reduced to as small as $5\lambda \times 5\lambda$ for $\lambda = 193$ nm, but note that $10\lambda \times 10\lambda$ is maintained for $\lambda \leq 47$ nm. The effects of varying domain size and cubic grid size for Geometry 2 have been investigated, noting less than 10 % intensity variations due to shrinking the domain size [44].

To verify trends observed of the scattering off 3-D periodic features from Fig. 5(b), related simulations have been performed using 2-D FDTD. All simulation and imaging parameters are the same as those for the 3-D FDTD with three notable exceptions. First, the width of the FDTD domain is one-half of the unit cell size pictured in Figs. 2(b,h) for Geometry 1 and Geometry 2, respectively. Second, as a 2-D FDTD simulation, the depth of the domain along the y axis is ignored. Third, length of the cubic cells for all 2-D simulations is set to $\Delta s = 0.666666$ nm.

TABLE IV. FDTD domain size and length Δs of the cubic cells, for each geometry and wavelength.

λ (nm)	Geometry	x (nm)	y (nm)	z (nm)	Δs (nm)
13	1	672	720	280	1.000
	2	640	720	270	0.667
47	1	1344	1260	280	2.000
	2	640	720	270	0.667
122	1	1344	1260	280	2.000
	2	960	1080	270	0.667
157	1	1680	1800	280	2.000
	2	960	1080	270	0.667
193	1	2016	1980	280	2.000
	2	960	1080	270	0.667

Appendix B: Microscopy across the UV

To adequately convey microscopy challenges throughout the ultraviolet, a graphical comparison of realized optical microscopies is shown as Fig. 10. From the literature, the NA range should be treated as wavelength-dependent with the largest NA ranges obtained for $\lambda \geq 157$ nm. The National Institute of Standards and Technology (NIST) 193 nm microscope [56–59] features NA = 0.13 to 0.74. Shafer and Chuang patented catadioptric objective lens designs for both 193 nm and 157 nm, with implementations of NA = 0.8 having approximately an $\text{NA}_0 < 0.02$ [60]. Schuster patented refractive objective designs with NA < 0.85 for $\lambda = 157$ nm and $\lambda = 193$ nm [61]. An industrial imaging tool was reported by Eisner *et al.* with a variable NA of 0.60 to 0.92, in increments of 0.01 [62]. Switkes described immersion 157 nm optics with an NA of 1.3 [63].

For microscopy at $\lambda \leq 122$ nm, a catoptric lens limited to only two reflective elements is often required to minimize transmissivity losses at the cost of reduced NA range. Gelnert and Milster patented a 121.9 nm microscope for the Lyman- α line with a Schwarzschild-type catoptric lens of NA = 0.16 to 0.3 [64]. In the EUV, Glatzel, Franta, and colleagues described the design [65] and fabrication [66] of a $\lambda = 13.5$ nm Schwarzschild-type catoptric objective of NA = 0.15 to 0.5. Note however that in the EUV, other efforts utilize off-axis imaging such as Garletto *et al.* who discussed the development of an industrial imaging tool for the EUV with the effective NA defined by the reflectivity in an off-axis approach [67].

Appendix C: Estimating source intensities for Fig. 9

Photon counts for $\lambda \leq 157$ nm are estimated from the literature, relative to $\lambda = 193$ nm. A 157 nm laser typically has $10\times$ less fluence relative to similar 193 nm excimer sources [69]. Ar_2 -excimer light at $\lambda = 126$ nm is a comparable VUV source for estimating for $\lambda = 122$ nm. The total power of one conventional lamp is reportedly 10 mW [70] but recent Ar_2^* -excimer emitter have emission rates $10\times$ to $10^2\times$ larger [71]. From this, the estimated n_{ph} for $\lambda = 122$ nm is around $10^3\times$ less than that for $\lambda = 193$ nm. A $\lambda = 46.9$ nm laser with 13 $\bar{\text{I}}\text{J}$ pulses at a 10 Hz repetition rate has been demonstrated [72], yielding about $10^4\times$ less photons than a $\lambda = 193$ nm laser. A value of 64 photons per pixel per exposure has been reported for a detector in an EUV microscope [73], and it can be estimated that $\lambda = 13$ nm

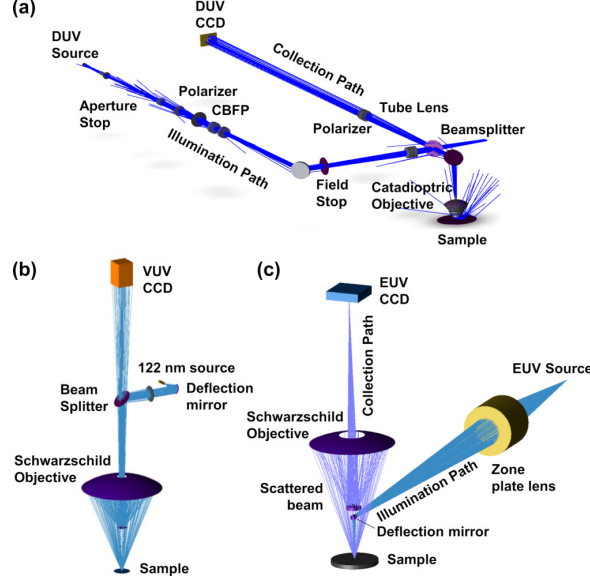


FIG. 10. Three schematic examples of the types of microscopes available in the DUV, VUV, and EUV, and simulation conditions for wavelength comparisons. (a) The NIST 193 nm microscope [59] represents the relatively high-NA values available at $\lambda = 193$ nm and historically at $\lambda = 157$ nm. (b) Gelnert and Milster at the University of Arizona patented a 121 nm microscope for the Lyman- α line with a Schwarzschild lens of approximately $NA = 0.16$ to 0.3 as pictured [64]. (c) A EUV (13.5 nm, 47 nm) dark-field microscope is shown based off a design published by RWTH Aachen University [68].

yields between $10^3 \times$ to $10^4 \times$ less photons. This intensity may increase as $\lambda = 13$ nm sources continue to develop.

The incident intensity of the NIST 193 nm Microscope at the sample has been calculated as $I_0(193 \text{ nm}) = 52000 \text{ W/m}^2$. The energy imparted on a 1 nm^2 sample area exposed for one second is $E = 5.3 \times 10^{-14} \text{ J}$. The energy of a single photon at $\lambda = 193 \text{ nm}$ is $E = 1.03 \times 10^{-18} \text{ J}$, meaning that per nm^2 per s the number of photons is 5.1×10^4 . This study assumes individual, square camera pixels each image a 4 nm^2 area at the sample, and 2×10^5 photons would be registered by one pixel over 1 s if the incident light is fully reflected into the image plane. While pixel size and exposure time are arbitrary, for simplicity we estimate $n_{\text{ph}}(193 \text{ nm}) = 2 \times 10^5$ at the sample which establishes the basis for Fig. 9 in

- [1] W. Bragg and A. Pippard, The form birefringence of macromolecules, *Acta Crystallographica* **6**, 865 (1953).
- [2] K. Zhang, Y. Tang, J. Meng, G. Wang, H. Zhou, T. Fan, and D. Zhang, Polarization-sensitive color in butterfly scales: polarization conversion from ridges with reflecting elements, *Optics Express* **22**, 27437 (2014).
- [3] N. Künzner, J. Diener, E. Gross, D. Kovalev, V. Y. Timoshenko, and M. Fujii, Form birefringence of anisotropically nanostructured silicon, *Phys. Rev. B* **71**, 195304 (2005).
- [4] L. A. Golovan, V. A. Melnikov, S. O. Konorov, A. B. Fedotov, V. Y. Timoshenko, A. M. Zheltikov, P. K. Kashkarov, D. A. Ivanov, G. I. Petrov, and V. V. Yakovlev, Linear and nonlinear optical anisotropy of amorphous oxidized silicon films induced by a network of pores, *Phys. Rev. B* **73**, 115337 (2006).
- [5] S.-H. Yang, M. L. Cooper, P. R. Bandaru, and S. Mookherjea, Giant birefringence in multi-slotted silicon nanophotonic waveguides, *Opt. Express* **16**, 8306 (2008).
- [6] K. Sinchuk, R. Dudley, J. D. Graham, M. Clare, M. Woldeyohannes, J. O. Schenk, R. P. Ingel, W. Yang, and M. A. Fiddy, Tunable negative group index in metamaterial structures with large form birefringence, *Optics Express* **18**, 463 (2010).
- [7] M. Yu, Y. Wang, W. Zhong, R. Guo, and X. Zhou, Optical properties of strongly anisotropic metamaterials, *Applied Physics A-Materials Science & Processing* **108**, 65 (2012).
- [8] M. Lorente-Crespo, G. C. Ballesteros, G. Goussetis, and C. Mateo-Segura, Experimental validation of all-dielectric mm-wave polarization conversion based on form birefringence, *IEEE Microwave and Wireless Components Letters* **26**, 759 (2016).
- [9] E. Brasselet, G. Gervinskas, G. Seniutinas, and S. Juodkazis, Topological shaping of light by closed-path nanoslits, *Phys. Rev. Lett.* **111**, 193901 (2013).
- [10] J. Cao, L. Mazerolles, M. Lancry, D. Solas, F. Brisset, and B. Poumellec, Form birefringence induced in multicomponent glass by femtosecond laser direct writing, *Optics Letters* **41**, 2739 (2016).
- [11] D. Meshulach, I. Dolev, Y. Yamazaki, K. Tsuchiya, M. Kaneko, K. Yoshino, and T. Fujii, Advanced lithography: wafer defect scattering analysis at DUV, *Proc. SPIE* **7638**,

- 10.1117/12.848326 (2010).
- [12] M. Born and E. Wolf, *Principles of optics: electromagnetic theory of propagation, interference and diffraction of light* (Cambridge Univ. Press, 1999).
 - [13] M. A. Kats, P. Genevet, G. Aoust, N. Yu, R. Blanchard, F. Aieta, Z. Gaburro, and F. Capasso, Giant birefringence in optical antenna arrays with widely tailorable optical anisotropy, *Proceedings of the National Academy of Sciences* **109**, 12364 (2012), <http://www.pnas.org/content/109/31/12364.full.pdf>.
 - [14] M. R. Shcherbakov, M. I. Dobynde, T. V. Dolgova, D.-P. Tsai, and A. A. Fedyanin, Full Poincaré sphere coverage with plasmonic nanoslit metamaterials at fano resonance, *Phys. Rev. B* **82**, 193402 (2010).
 - [15] J. Bar-David, L. Stern, and U. Levy, Dynamic control over the optical transmission of nanoscale dielectric metasurface by alkali vapors, *Nano Letters* **17**, 1127 (2017).
 - [16] M. Khorasaninejad and F. Capasso, Broadband multifunctional efficient meta-gratings based on dielectric waveguide phase shifters, *Nano Letters* **15**, 6709 (2015), pMID: 26372331, <https://doi.org/10.1021/acs.nanolett.5b02524>.
 - [17] Y. Ra'di, D. L. Sounas, and A. Alù, Metagratings: Beyond the limits of graded metasurfaces for wave front control, *Phys. Rev. Lett.* **119**, 067404 (2017).
 - [18] V. Popov, F. Boust, and S. N. Burokur, Controlling diffraction patterns with metagratings, *Phys. Rev. Applied* **10**, 011002 (2018).
 - [19] F. Liu, O. Tsilipakos, A. Pitilakis, A. C. Tasolamprou, M. S. Mirmoosa, N. V. Kantartzis, D.-H. Kwon, M. Kafesaki, C. M. Soukoulis, and S. A. Tretyakov, Intelligent metasurfaces with continuously tunable local surface impedance for multiple reconfigurable functions, *Phys. Rev. Applied* **11**, 044024 (2019).
 - [20] D. R. Smith, D. C. Vier, T. Koschny, and C. M. Soukoulis, Electromagnetic parameter retrieval from inhomogeneous metamaterials, *Phys. Rev. E* **71**, 036617 (2005).
 - [21] R. A. Shelby, D. R. Smith, and S. Schultz, Experimental verification of a negative index of refraction, *Science* **292**, 77 (2001).
 - [22] M. Beresna, M. Gecevicius, P. G. Kazansky, and T. Gertus, Radially polarized optical vortex converter created by femtosecond laser nanostructuring of glass, *App Phys Lett* **98**, 10.1063/1.3590716 (2011).
 - [23] M. Beresna, M. Gecevicius, and P. G. Kazansky, Ultrafast laser direct writing and

- nanostructuring in transparent materials, *Advances in Optics and Photonics* **6**, 293 (2014).
- [24] A. Cerkaskaite, R. Drevinskas, A. Solodar, I. Abdulhalim, and P. G. Kazansky, Form-birefringence in ITO thin films engineered by ultrafast laser nanostructuring, *ACS Photonics* **4**, 2944 (2017).
 - [25] L. Vertchenko, E. Shkondin, R. Malureanu, and C. Monken, Laguerre-gauss beam generation in IR and UV by subwavelength surface-relief gratings, *Optics Express* **25**, 5917 (2017).
 - [26] B. M. Barnes, L. P. Howard, J. Jun, P. Lipscomb, and R. M. Silver, Zero-order imaging of device-sized overlay targets using scatterfield microscopy, *Proc SPIE* **6518**, 65180F (2007).
 - [27] H. J. Patrick, R. Attota, B. M. Barnes, T. A. Germer, R. G. Dixon, M. T. Stocker, R. M. Silver, and M. R. Bishop, Optical critical dimension measurement of silicon grating targets using back focal plane scatterfield microscopy, *Journal of Micro-Nanolithography MEMS and MOEMS* **7**, 10.1117/1.2885275 (2008).
 - [28] R. M. Silver, B. M. Barnes, R. Attota, J. Jun, M. Stocker, E. Marx, and H. J. Patrick, Scatterfield microscopy for extending the limits of image-based optical metrology, *Appl Opt* **46**, 4248 (2007).
 - [29] B. M. Barnes, R. Attota, R. Quintanilha, Y.-J. Sohn, and R. M. Silver, Characterizing a scatterfield optical platform for semiconductor metrology, *Measurement Science and Technology* **22**, 10.1088/0957-0233/22/2/024003 (2011).
 - [30] B. M. Barnes, M. Y. Sohn, F. Goasmat, H. Zhou, A. E. Vladar, R. M. Silver, and A. Arceo, Three-dimensional deep sub-wavelength defect detection using $\lambda=193$ nm optical microscopy, *Optics Express* **21**, 26219 (2013).
 - [31] B. M. Barnes, F. Goasmat, M. Y. Sohn, H. Zhou, R. M. Silver, and A. Arceo, Enhancing 9 nm node dense patterned defect optical inspection using polarization, angle, and focus, *Proc SPIE* **8681**, 86810E (2013).
 - [32] B. M. Barnes, F. Goasmat, M. Y. Sohn, H. Zhou, A. E. Vladar, and R. M. Silver, Effects of wafer noise on the detection of 20-nm defects using optical volumetric inspection, *Journal of Micro-Nanolithography MEMS and MOEMS* **14**, 9 (2015).
 - [33] J. Qin, R. M. Silver, B. M. Barnes, H. Zhou, and F. Goasmat, Fourier domain optical tool normalization for quantitative parametric image reconstruction, *Appl. Opt.* **52**, 6512 (2013).
 - [34] J. Qin, R. M. Silver, B. M. Barnes, H. Zhou, R. G. Dixon, and M. A. Henn, Deep subwavelength nanometric image reconstruction using Fourier domain optical normalization,

- Light-Science & Applications **5**, e16038 (2016).
- [35] B. A. Palmer, G. R. Edwards-Gau, B. M. Kariuki, K. D. M. Harris, I. P. Dolbnya, and S. P. Collins, X-ray birefringence imaging, *Science* **344**, 1013 (2014), <https://science.sciencemag.org/content/344/6187/1013.full.pdf>.
 - [36] M. Lapedus, Finding defects is getting harder, <http://semiengineering.com/finding-killer-defects/> (2015).
 - [37] Y. ho Chuang, J. J. Armstrong, Y. Deng, J. D. Liou, V. Dribinski, and J. Fielden, 193nm laser and inspection system, U.S. Patent No. 9,529,182 (2016).
 - [38] R. M. Silver, B. M. Barnes, Y. Sohn, R. Quintanilha, H. Zhou, C. Deeb, M. Johnson, M. Goodwin, and D. Patel, The limits and extensibility of optical patterned defect inspection, *Proc SPIE* **7638**, 7638 (2010).
 - [39] B. M. Barnes, Y. J. Sohn, F. Goasmat, H. Zhou, R. M. Silver, and A. Arceo, Scatterfield microscopy of 22 nm node patterned defects using visible and DUV light, *Proc SPIE* **8324**, 83240F (2012).
 - [40] T. A. Germer, K. A. Sharma, T. G. Brown, and J. B. Oliver, Polarized optical scattering by inhomogeneities and surface roughness in an anisotropic thin film, *J. Opt. Soc. Am. A* **34**, 1974 (2017).
 - [41] A. Singh, G. Sharma, N. Ranjan, K. Mittholiya, A. Bhatnagar, B. P. Singh, D. Mathur, and P. Vasa, Controlling material birefringence in sapphire via self-assembled, sub-wavelength defects, *Applied Physics B-Lasers and Optics* **124**, 10.1007/s00340-018-6892-2 (2018).
 - [42] S. Natarajan, A 14nm logic technology featuring 2nd-generation FinFET, air-gapped interconnects, self-aligned double patterning and a 0.0588 mm² SRAM cell size, in *2014 IEEE International Electron Devices Meeting* (2014) pp. 3.7.1–3.7.3.
 - [43] B. Barnes, Geometries and material properties for simulating semiconductor patterned bridge defects using the finite-difference time-domain (FDTD) method, <http://doi.org/10.18434/T4/1500937> (2018).
 - [44] B. M. Barnes, H. Zhou, M. A. Henn, M. Y. Sohn, and R. M. Silver, Optimizing image-based patterned defect inspection through FDTD simulations at multiple ultraviolet wavelengths, *Proc SPIE* **10330**, 103300W (2017).
 - [45] K. Yee, Numerical solution of initial boundary value problems involving Maxwell’s equations in isotropic media, *IEEE Trans Antennas Propag* **14**, 302 (1966).

- [46] H. Piller, Silicon (amorphous) (a-Si), in *Handbook of Optical Constants of Solids*, edited by E. D. Palik (Academic Press, Boston, 1985) pp. 571–586.
- [47] D. F. Edwards, Silicon (Si)*, in *Handbook of Optical Constants of Solids*, edited by E. D. Palik (Academic Press, Boston, 1985) pp. 547–569.
- [48] H. R. Philipp, Silicon dioxide (SiO₂), type (crystalline), in *Handbook of Optical Constants of Solids*, edited by E. D. Palik (Academic Press, Boston, 1985) pp. 719–747.
- [49] E. Filatova, A. Sokolov, J.-M. André, F. Schaefer, and W. Braun, Optical constants of crystalline HfO₂ for energy range 140–930 eV, *Appl Opt* **49**, 2539 (2010).
- [50] D. Franta, D. Nečas, I. Ohlídal, and A. Giglia, Dispersion model for optical thin films applicable in wide spectral range, *Proc SPIE* **9628**, 96281U (2015).
- [51] Q.-J. Liu, N.-C. Zhang, F.-S. Liu, and Z.-T. Liu, Structural, electronic, optical, elastic properties and born effective charges of monoclinic HfO₂ from first-principles calculations, *Chinese Physics B* **23**, 047101 (2014).
- [52] I. Richter, P. Sun, F. Xu, and Y. Fainman, Design considerations of form birefringent microstructures, *Applied Optics* **34**, 2421 (1995).
- [53] S. Knight, R. Dixon, R. L. Jones, E. K. Lin, N. G. Orji, R. Silver, J. S. Villarrubia, A. E. Vladar, and W.-L. Wu, Advanced metrology needs for nanoelectronics lithography, *Comptes Rendus Physique* **7**, 931 (2006).
- [54] K. Wells, G. Chen, M. Derstine, S. Lange, and D. Shortt, Extending optical inspection to the VUV, in *2017 International Conference on Frontiers of Characterization and Metrology for Nanoelectronics (FCMN)*, edited by D. G. Seiler (NIST, Monterey, CA USA, 2017) pp. 92–101.
- [55] B. M. Barnes, H. Zhou, M.-A. Henn, M. Y. Sohn, and R. M. Silver, Assessing the wavelength extensibility of optical patterned defect inspection, *Proc SPIE* **10145**, 1014516 (2017).
- [56] Y. J. Sohn, B. M. Barnes, L. Howard, R. M. Silver, R. Attota, and M. T. Stocker, Köhler illumination for high-resolution optical metrology, *Proc SPIE* **6152**, 61523S (2006).
- [57] Y. Sohn and R. M. Silver, Köhler illumination analysis for high-resolution optical metrology using 193 nm light, *Proc SPIE* **6518**, 65184V (2007).
- [58] Y. J. Sohn, R. Quintanilha, B. M. Barnes, and R. M. Silver, 193 nm angle-resolved scatterfield microscope for semiconductor metrology, *Proc SPIE* **7405**, 74050R (2009).
- [59] M. Y. Sohn, B. M. Barnes, and R. M. Silver, Design of angle-resolved illumination optics

- using nonimaging bi-telecentricity for 193nm scatterfield microscopy, *Optik (Stuttgart)* **156**, 635 (2018).
- [60] Y.-H. Chuang and D. Shafer, Broad band DUV, VUV long-working distance catadioptric imaging system, U.S. Patent No. 7,136,234 (14 Nov. 2006).
- [61] K.-H. Schuster, Very high-aperture projection objective, U.S. Patent No. 7,203,008 (24 Feb 2009).
- [62] K. Eisner, P. Kuschnerus, J.-P. Urbach, C. M. Schilz, T. Engel, A. M. Zibold, T. Yasui, and I. Higashikawa, Aerial image measurement system for 157 nm lithography, *Proc SPIE* **4889**, 469 (2002).
- [63] M. Switkes, T. M. Bloomstein, M. Rothschild, E. W. Arriola, and T. H. Morrison, A 157-nm immersion microstepper, *Proc SPIE* **5754**, 237 (2005).
- [64] B. Gelernt and T. D. Milster, Apparatus and method for deep ultraviolet optical microscopy, U.S. Patent No. 8,472,111 (25 Jun. 2013).
- [65] H. Glatzel, D. Ashworth, M. Bremer, R. Chin, K. Cummings, L. Girard, M. Goldstein, E. Gullikson, R. Hudyma, J. Kennon, B. Kestner, L. Marchetti, P. Naulleau, R. Soufli, and E. Spiller, Projection optics for extreme ultraviolet lithography (EUVL) micro-field exposure tools (METs) with a numerical aperture of 0.5, *Proc SPIE* **8679**, 867917 (2013).
- [66] H. Glatzel, D. Ashworth, D. Bajuk, M. Bjork, M. Bremer, M. Cordier, K. Cummings, L. Girard, M. Goldstein, E. Gullikson, *et al.*, Projection optics for euvl micro-field exposure tools with 0.5 na, *Proc. SPIE* **9048**, 90481K (2014).
- [67] A. Garetto, T. Scherübl, and J. H. Peters, Aerial imaging technology for photomask qualification: from a microscope to a metrology tool, *Advanced Optical Technologies* **1**, 289 (2012).
- [68] A. Maryasov, S. Herbert, L. Juschkin, R. Lebert, and K. Bergmann, EUV actinic mask blank defect inspection: results and status of concept realization, *Proc SPIE* **7985**, 79850C (2011).
- [69] J. Ihlemann, M. Schulz-Ruhtenberg, and T. Fricke-Begemann, Micro patterning of fused silica by ArF- and F₂-laser ablation, *Journal of Physics: Conference Series* **59**, 206 (2007).
- [70] H. Kang, A. Bourov, and B. W. Smith, Optical lithography at a 126-nm wavelength, *Proc SPIE* **4343**, 797 (2001).
- [71] A. A. Chistyakov, G. E. Kotkovskii, A. V. Sychev, A. N. Perederiy, Budovich, V. L., and D. V. Budovich, An excimer-based FAIMS detector for detection of ultra-low concentration

- of explosives, Proc SPIE **9072**, 907211 (2014).
- [72] S. Heinbuch, M. Grisham, D. Martz, and J. J. Rocca, Demonstration of a desk-top size high repetition rate soft x-ray laser, Optics Express **13**, 4050 (2005).
- [73] A. Wojdyla, A. Donoghue, M. P. Benk, P. P. Naulleau, and K. A. Goldberg, Aerial imaging study of the mask-induced line-width roughness of EUV lithography masks, Proc SPIE **9776**, 97760H (2016).